

## Article

# Petrogenesis of the Qiongduojiang Gabbro in Tethys Himalaya and Its Metallogenetic Implication

Jianzhong Li <sup>1,2</sup>, Yong Huang <sup>2,\*</sup>, Qingsong Wu <sup>2,3</sup>, Li Zhang <sup>4</sup>, Tao Xiong <sup>2</sup>, Bing Wang <sup>2</sup>, Zhiqiang Liang <sup>2</sup>, Huawen Cao <sup>4</sup> , Wei Liang <sup>4</sup> and Zuowen Dai <sup>5</sup>

<sup>1</sup> School of Earth Sciences, Chengdu University of Technology, Chengdu 610059, China

<sup>2</sup> Research Center of Applied Geology, China Geological Survey, Chengdu 610036, China

<sup>3</sup> School of Engineering, China University of Geosciences, Wuhan 430074, China

<sup>4</sup> Cheng Center, China Geological Survey, Chengdu 611230, China; zhangli@mail.cgs.gov.cn (L.Z.)

<sup>5</sup> School of Civil and Resource Engineering, University of Science and Technology Beijing, Beijing 100083, China

\* Correspondence: yong.huang@hotmail.com or huangy@mail.cgs.gov.cn; Tel.: +86-18086828841

**Abstract:** With the northward subduction and final closure of the Neo-Tethyan oceanic crust, the Indian and Eurasian plates finally collided together and underwent a strong collision orogenic event, resulting in large-scale crust–mantle magmatic interactions. In order to clarify the controversies about tectono-magmatic activities after the Indian–Eurasian continental collision, we report the newly dated Eocene Qiongduojiang gabbro explored in the Tethyan–Himalaya belt, southern Tibet. LA-ICP-MS zircon U–Pb dating shows that the crystallization age of the Qiongduojiang gabbro is  $46.1 \pm 1.7$  Ma. The whole-rock major and trace elements, as well as Rb–Sr, Sm–Nd, and Pb isotopic data results, show that the Qiongduojiang gabbro is apparently depleted in Nd isotopes, is enriched in Pb isotopes, and has maintained a consistent  $^{87}\text{Sr}/^{86}\text{Sr}(t)$  value. This paper argues that the E–MORB-like Qiongduojiang gabbro originated from asthenosphere upwelling caused by slab breakoff of the Neo-Tethyan oceanic plate. This event caused large-scale magmatic activities, a magmatic mixing process between ancient crust and deep mantle, and wild distribution of Eocene Gangdese plutons along the Yarlung–Tsangpo Suture Zone, and it rendered the subduction-modified Tibetan lithosphere fertile from the Gangdese porphyry Cu deposits.

**Keywords:** Qiongduojiang gabbro; Eocene; Tethyan–Himalaya belt; Tibet; slab breakoff; porphyry Cu deposits



**Citation:** Li, J.; Huang, Y.; Wu, Q.; Zhang, L.; Xiong, T.; Wang, B.; Liang, Z.; Cao, H.; Liang, W.; Dai, Z. Petrogenesis of the Qiongduojiang Gabbro in Tethys Himalaya and Its Metallogenetic Implication. *Minerals* **2023**, *13*, 721. <https://doi.org/10.3390/min13060721>

Academic Editors: Majid Ghaderi, Huan Li, Kotaro Yonezu and Sung Hi Choi

Received: 27 March 2023

Revised: 22 May 2023

Accepted: 23 May 2023

Published: 24 May 2023



**Copyright:** © 2023 by the authors. Licensee MDPI, Basel, Switzerland. This article is an open access article distributed under the terms and conditions of the Creative Commons Attribution (CC BY) license (<https://creativecommons.org/licenses/by/4.0/>).

## 1. Introduction

As the roof of the world, the Tibetan Plateau was formed by the northward-directed subduction of the Neo-Tethyan oceanic slab beneath the Asian continent starting around the Late Triassic–Early Jurassic [1–6] and subsequent Indian–Asian continental collision [7–11]. However, although tremendous efforts have been made to decipher the tectono-magmatic evolution history along the Yarlung–Tsangpo Suture Zone (YTSZ), interpretations of ages and corresponding geodynamic settings of magmatism in this area are still controversial. For example, Zhou et al. [12] suggested that the Neo-Tethyan slab rollback, Neo-Tethyan slab breakoff, and ongoing India–Asia collision occurred at approximately 69–53 Ma, 53–49 Ma, and 49–43 Ma, respectively, whereas Shui et al. [13] advocated that the Gangdese belt may still have been an active continental margin until ca. 41 Ma, followed by the Indian–Eurasian collision. One of the most popular models is that during 55–45 Ma, the Neo-Tethyan slab breakoff caused an upwelling of the asthenospheric mantle, which offered heat and material to form a magmatic flare-up event in the Gangdese belt [14–19]. Kohn and Parkinson [20] suggested that the slab breakoff occurred at approximately 42 Ma, which coincides with the termination of the Gangdese arc magmatism [21]. Gao et al. [10] and Xu et al. [22] advocated that the slab breakoff formed intraplate-type mafic magmas in the Lhasa terrane at 42–38 Ma.

After the slab breakoff model was proposed by Davies and von Blanckenburg [23] and von Blanckenburg and Davies [24], studies adopted this model to explain magmatic flare-ups [25], exhumation of high-pressure metamorphic rocks [26], and rapid topographic uplift [27]. Niu [28] argued that due to the big density difference between granitic gneisses and mantle, exhumation of eclogite-facies continental crust may not necessarily be related to slab breakoff. Freeburn et al. [29] modeled the collision of two continental plates following a period of oceanic subduction, and the results show that asthenospheric melting triggered by metamorphic water derived from the slab tip is short-lived and hard to recognize in the geological record. Indeed, besides Ji et al. [30], who reported slab breakoff related oceanic island basalt (OIB)-type Langshan gabbros from the Gyangze region of the eastern Tethys, few studies have demonstrated asthenospheric-derived mafic rocks as a direct response to the Neo-Tethyan slab breakoff in southern Tibet [22].

In this study, we found a gabbro outcrop in the Qiongduojiang area of the Tethys belt. LA-ICP-MS zircon U-Pb dating; whole-rock geochemistry; and Rb-Sr, Sm-Nd, and Pb isotopic analyses were used to: (1) precisely constrain the age of Qiongduojiang gabbro, (2) investigate its magma sources and coeval magmatism, (3) deduce the possible geodynamic setting when Qiongduojiang gabbro formed, and (4) decipher the role of magmas that the Qiongduojiang gabbro represented in the Gangdese porphyry Cu mineralization. The conclusion of this study combined with other geological evidence is able to better unravel the tectono-magmatic evolution history and metallogenetic model of southern Tibet.

## 2. Geological Background

From north to south, the Tibet Plateau consists of Songpan–Ganzi terrane, Qiangtang terrane, Lhasa terrane, and Himalayan terrane. They are separated by the Jinsha River Suture Zone, the Bangong–Nujiang Suture Zone, and YTSZ, respectively [31]. Since the Late Triassic, marine sedimentary sequences have been deposited, mainly including Triassic, Jurassic, and Cretaceous argillaceous sandstone, sand shale, carbonaceous slate, and marl [32,33]. A long and narrow ophiolitic mélangé belt is distributed on the northern margin of Tethys Himalaya. The main body of this mélangé belt is bounded by the Yajiang ophiolite belt to the south and the Qiongduojiang fault to the north. A large number of residual oceanic crust materials are involved in the ophiolitic mélangé belt. The main matrix is Triassic deep-sea-debris sedimentary rocks. This mélangé belt can represent the real subducted oceanic crust of the Neo-Tethyan ocean. The deformation of Yajiang ophiolite is weak, and the main body tilts to the south, which may represent a small forearc extensional ocean basin formed in the process of ocean subduction. Since the Late Triassic, the Tethys Himalayan belt has been in the passive continental margin of the northern margin of the Indian terrane [31] (Figure 1).

The Tethys Himalayan belt is located south of the YTSZ and north of the high Himalayan crystalline rock series. The Tethys Himalayan Sequence includes a southern zone that consists of Palaeozoic to Eocene platform carbonates and terrigenous units [34,35], and a northern zone that is dominated by a Mesozoic to Palaeocene outer shelf, continental slope, and rise deposits [36]. Affected by the regional extension and detachment structure, a metamorphic core complex belt exists that is composed of a series of plutonic intrusive rocks and metamorphic sedimentary rocks. Large-scale Cambrian gneiss domes (such as the Malashan, Peikuco, Lhagoi Kangri, Mabja–Sakya, Kampa, Kangmar, Ramba, and Yardoï from west to east) and Cenozoic leucogranite are exposed in the core of the metamorphic core complex [37].

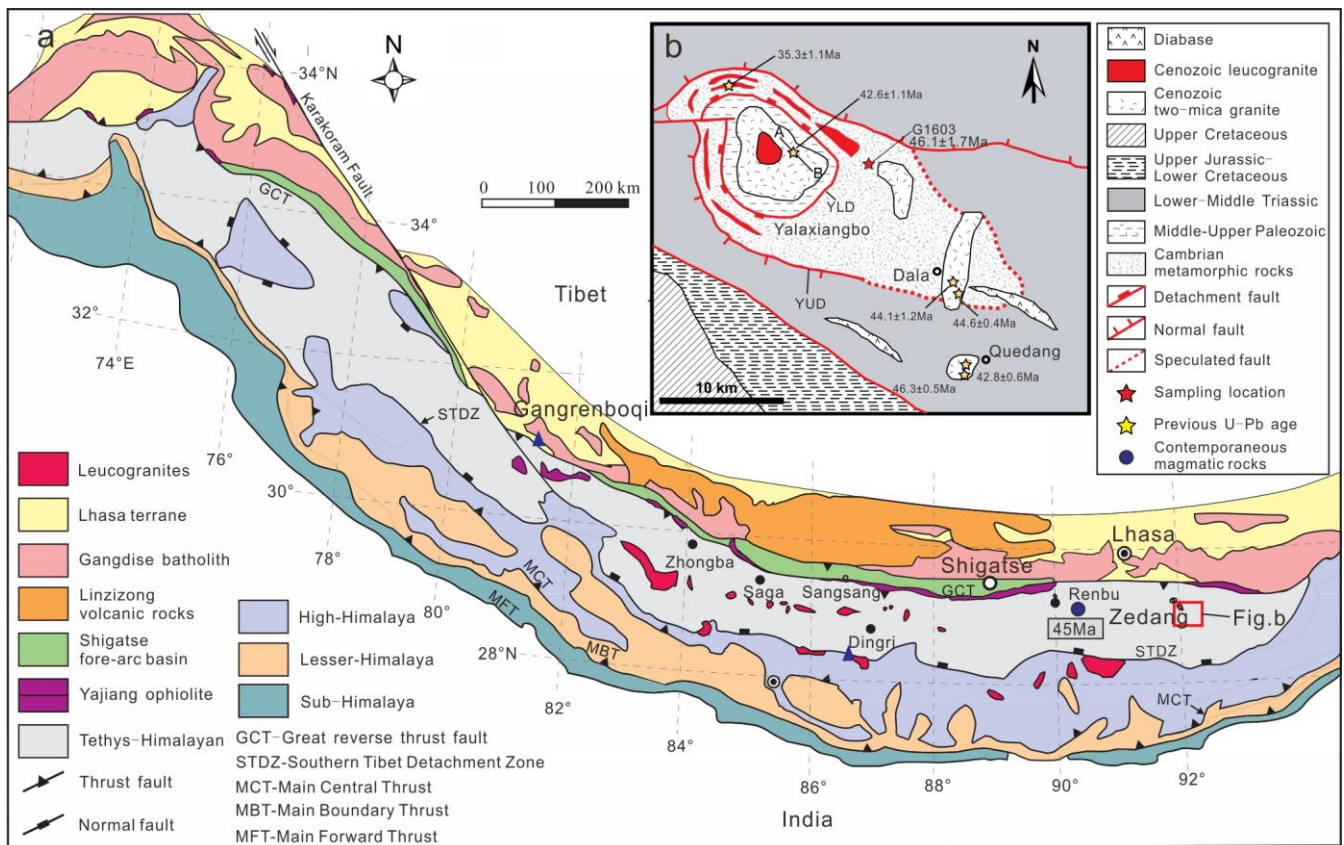


**Figure 1.** (a) Simple Geological Map of Gangdese–Himalaya [7]. (b) Simple Geological Map of the Yalaxiangbo gneiss dome and the sampling location of Qiongduojiang gabbro, south Tibet [19]. YLD: Yardoi lower detachment; YUD: Yardoi upper detachment.

The Yardoi dome is located 40 km to the south of the Gangdese Thrust and 100 km to the north of the South Tibetan Detachment System (STDS). The crystalline basement rocks of the Yardoi are amphibolite, garnet-bearing metapelite, garnet–graphite schist, augen gneiss, and minor epidote and pyroxenite [38]. Cenozoic granitic rocks of various ages intrude into these basement rocks and Triassic sediment [19] (Figure 1b). Two-mica granitic rocks with ages of ca. 44–43 Ma occur in the center of the YGD, Dala, and Quedang area and have undergone minor shear, whereas sub-parallel meter-thick granitic dykes ( $35.3 \pm 1.1$  Ma) that intruded the garnet–graphite schist seem undeformed internally and have intruded the high-grade metamorphic rocks and the two-mica granites [39]. Structurally, the litho-tectonic units of dome mantle, rim, and covering sequences are separated by the Yardoi lower detachment (YLD) and the Yardoi upper detachment (YUD), respectively [37] (Figure 1b). Three stages of Kinematical activities have deformed the Yardoi dome [37]. The S–C fabrics in the orthogneiss recorded a top-to-the-SSE shear (D1); S–C fabrics in pelitic phyllite, asymmetric pressure shadows around garnet porphyroblasts, asymmetric leucogranite pudding in the dome mantle, and asymmetric folds in pelitic schist/phyllite indicated a top-to-the-NNW shear (D2); and mineral fibers and steps on slickenside and normal faults or fractures offsetting earlier deformations represent top-down-to-outward faulting (D3).

The Qiongduojiang gabbro samples collected in this study are located at the edge of the Yardoi metamorphic core complex. The sampling coordinates are  $92^{\circ}6.75'$  E and  $28^{\circ}52.35'$  N (Figure 1b). This Gabbro dyke, with 2–3 m width and 50–70 m length, intrudes into the Cambrian schist with NW trending. The Qiongduojiang gabbro consists of clinopyroxene (25%–30%), amphibole (30%–45%), plagioclase (5%–10%), biotite (15%–20%), and quartz (1%–5%) (Figure 2). The accessory minerals are ilmenite, magnetite, and sphene.

Weak carbonation and mylonite structures can be seen that is locally affected by later tectonic activities.

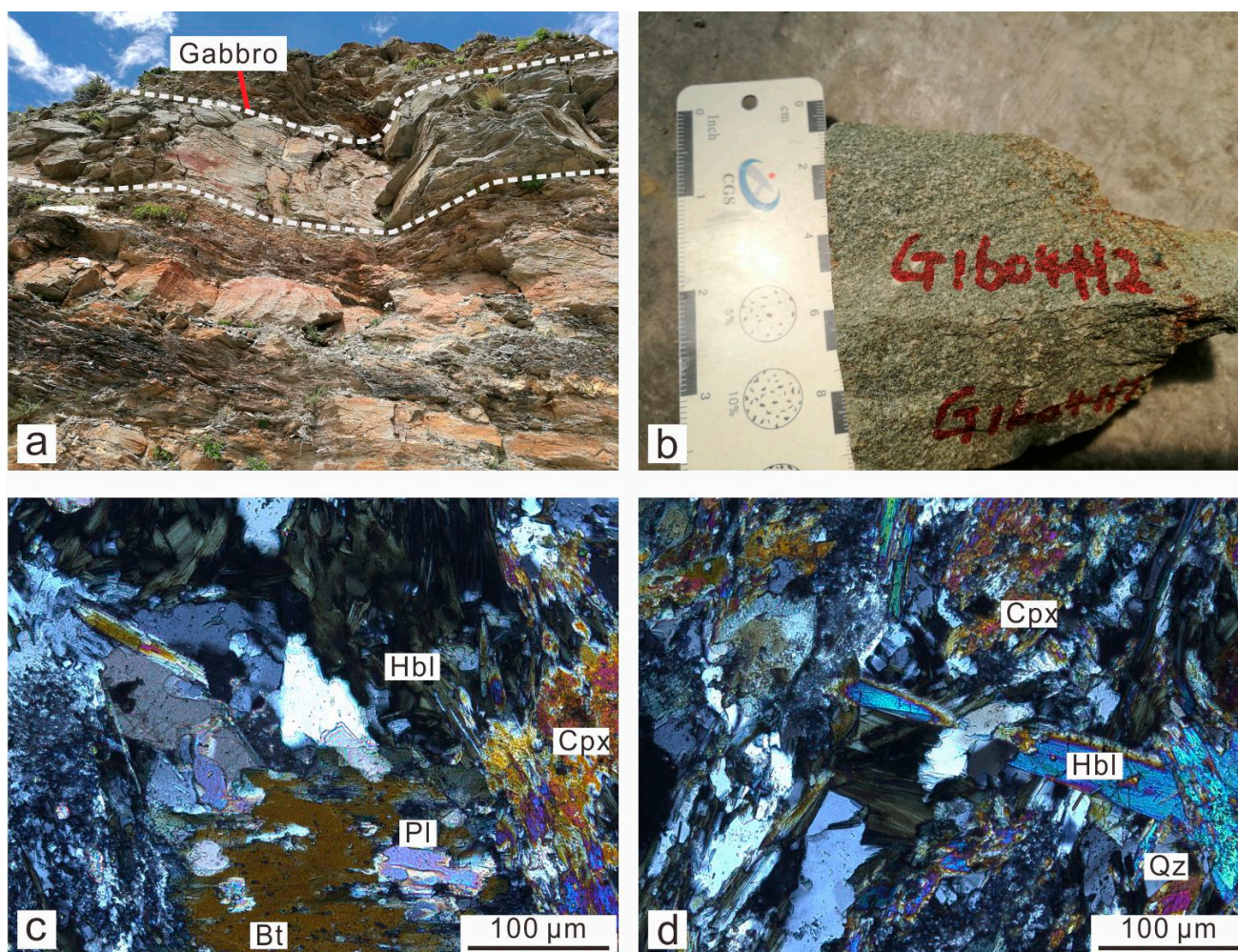


**Figure 2.** (a) Outcrop and (b) hand sample photographs; (c,d) micrographs under cross-polarized light of the Qiongduojiang gabbro. Abbreviation: Hbl = Hornblende, Cpx = Clinopyroxene, Pl = Plagioclase, Qz = Quartz, Bt = Biotite.

### 3. Analysis Methods

Zircon minerals are separated by Langfang Chengxin Geological Service Company, Hebei, China. The selected zircon minerals were placed in the epoxy resin mount and then polished. After cathodoluminescence (CL) photographic analysis, overgrowth rims of zircon without inclusions and cracks were selected for U-Pb dating. Zircon age was determined via laser ablation inductively coupled plasma mass spectrometry in the laboratory of China University of Geosciences (Beijing). In the experiment, He gas is used as the carrier gas of a denuded material. Laser ablation conditions were  $4 \text{ J/cm}^2$  of laser energy, 8 Hz of ablation frequency, and  $33 \text{ }\mu\text{m}$  of spot diameter. Zircon 91500 and NIST SRM612 were used as external standards. The error of single test data and the weighted average error of  $^{206}\text{Pb}/^{238}\text{U}$  age are  $1\sigma$ . Details of the analytical processes were described by [40]. Data processing was conducted by the software of ICPMSDataCal [40] and plotted by Isoplot 3.0 [41]. The test results are listed in Table 1.

**Table 1.** LA-ICP-MS zircon U-Pb ages of Qiongduojiang gabbro in Tethys–Himalayan.

Measure Point	Th	U	Th/U	The Isotopic Ratio (The Error 1σ)						Age (Ma)			
				<sup>207</sup> Pb/ <sup>206</sup> Pb	1σ	<sup>207</sup> Pb/ <sup>235</sup> U	1σ	<sup>206</sup> Pb/ <sup>238</sup> U	1σ	<sup>207</sup> Pb/ <sup>235</sup> U	1σ	<sup>206</sup> Pb/ <sup>238</sup> U	1σ
1	278.2	1080.6	0.3	0.1802	0.0057	12.6853	0.3962	0.4964	0.0075	2656.6	29.5	2598.7	32.5
2	1963.7	1626.8	1.2	0.0491	0.0084	0.0483	0.0063	0.0075	0.0004	48.0	6.1	48.6	2.2
3	2631.3	3077.9	0.9	0.0464	0.0022	0.2160	0.0099	0.0327	0.0005	198.6	8.3	207.4	3.4
4	1802.8	2890.0	0.6	0.0503	0.0022	0.2391	0.0101	0.0336	0.0006	217.7	8.3	212.9	3.8
5	663.9	1602.4	0.4	0.1479	0.0052	8.3161	0.2749	0.3964	0.0067	2266.1	30	2152.5	30.9
6	329.9	1342.1	0.2	0.1771	0.0057	12.7239	0.3921	0.5077	0.0081	2659.4	29.1	2646.6	34.7
7	198.6	1131.0	0.2	0.0611	0.0027	0.8035	0.0361	0.0930	0.0016	598.8	20.3	573.3	9.4
8	21.4	706.2	0.0	0.2271	0.0072	17.3452	0.5434	0.5429	0.0083	2954.1	30.1	2795.4	34.7
9	306.3	904.8	0.3	0.2095	0.0163	15.6004	2.8089	0.5328	0.0693	2852.6	171.8	2753.3	291.3
10	476.5	578.7	0.8	0.2673	0.0168	18.9546	1.1611	0.5715	0.0431	3039.5	59.1	2914.2	176.6
11	1367.8	4088.1	0.3	0.0558	0.0029	0.2773	0.0134	0.0358	0.0007	248.5	10.7	226.9	4.2
12	4822.7	6806.0	0.7	0.0575	0.0022	0.5873	0.0218	0.0734	0.0012	469.1	13.9	456.4	7.4
13	683.7	2959.0	0.2	0.0561	0.0025	0.6357	0.0286	0.0811	0.0016	499.6	17.7	502.8	9.3
14	15,353.7	5441.5	2.8	0.0472	0.0020	0.1206	0.0052	0.0184	0.0003	115.6	4.7	117.3	2.0
15	323.0	447.7	0.7	0.0703	0.0037	1.6114	0.0867	0.1643	0.0033	974.6	33.7	980.8	18.5
16	589.9	1480.9	0.4	0.0572	0.0028	0.5637	0.0275	0.0711	0.0016	453.9	17.8	442.7	9.3
17	1000.3	2131.9	0.5	0.0562	0.0022	0.7486	0.0295	0.0952	0.0014	567.4	17.2	586.1	8.0
18	242.2	1922.9	0.1	0.0571	0.0035	0.7760	0.0423	0.0980	0.0016	583.2	24.2	602.9	9.3
19	2494.9	2792.3	0.9	0.0531	0.0023	0.5112	0.0212	0.0690	0.0011	419.2	14.3	430.0	6.4
20	583.9	3154.5	0.2	0.0567	0.0025	0.8452	0.0362	0.1070	0.0019	622.0	19.9	655.0	11.2
21	69,303.4	10,385.0	6.7	0.0507	0.0032	0.0489	0.0031	0.0069	0.0002	48.5	3.0	44.5	1.3
22	77,796.0	19,327.5	4.0	0.0461	0.0070	0.0502	0.0100	0.0076	0.0006	49.7	9.7	48.7	4.0
23	95,789.1	16,794.2	5.7	0.0431	0.0061	0.0485	0.0027	0.0073	0.0004	48.1	2.7	47.1	2.2
24	6686.4	7056.0	0.9	0.0549	0.0076	0.0534	0.0051	0.0075	0.00047	52.8	4.9	47.9	3.0
25	13,178.3	4284.1	3.1	0.0561	0.0088	0.0565	0.0087	0.0079	0.0009	55.8	8.3	50.7	5.8
26	16,812.6	6073.9	2.8	0.0537	0.0074	0.0490	0.0052	0.0069	0.0004	48.6	5.0	44.5	2.2
27	31,242.0	12,358.4	2.5	0.0495	0.0027	0.1096	0.0056	0.0162	0.0004	105.6	5.1	103.7	2.8

The whole-rock major and trace elements were analyzed by Analytical Laboratory Beijing Research Institute of Uranium Geology (ALBRIUG). Rock samples were first pulverized to powder to pass through 200 mesh (75 μm) prior to mineral analysis and element distributions. Then, the powdered samples were dried at 105 °C for 2 h. The major elements were analyzed via XRF (Philips PW2404) on fused glass beads with an excitation condition of 50 kV/50 mA and a 30 mm diameter of viewed light beam. Gravimetry was used to measure the loss on ignition when the samples were heated to a temperature of 1100 °C. For trace element analysis, 50 mg of sample powder was dissolved in distilled HNO<sub>3</sub> + HF and then ultrasonically stirred. Thereafter, the solutions were evaporated to dryness, and the residue was dissolved with HNO<sub>3</sub> + HF. Subsequently, the solutions were heated at 130 °C for 3 h, and the solutions were diluted to 50 mL by using ultrapure H<sub>2</sub>O. Those solutions were analyzed by Element XR inductively coupled plasma mass spectrometry (Element XR/ICP-MS). The analysis accuracy is better than 5% for major elements and 5%–10% for trace elements. The whole-rock geochemical data are listed in Table 2. The Rb-Sr, Sm-Nd, and Pb isotopes of the whole rock were also completed by ALBRIUG. The samples were ground to 200 mesh and reduced to 10 g. The samples were analyzed in the oven and dried at 80 °C for 3 h. The samples were dissolved with hydrofluoric acid and perchloric acid. Rb and Sr were separated and purified via the cation resin exchange method. The isotopic compositions of Rb and Sr were analyzed via thermoelectric ion mass spectrometer MAT261. The Nd isotope ratio mass spectrometry analysis is completed by the thermal ionization mass spectrometer Triton. The mass fractionation generated in the mass spectrometry analysis is corrected by the power law with  $n(^{146}\text{Nd})/n(^{144}\text{Nd}) = 0.7219$ . The Sm and Nd contents are calculated by the isotope dilution formula. The whole analysis process is monitored by GBW04419 ( $^{143}\text{Nd}/^{144}\text{Nd} = 0.512722 \pm 0.000006$ ) and JNdi-1 ( $^{143}\text{Nd}/^{144}\text{Nd} = 0.512115 \pm 0.000005$ ) reference materials, respectively. The determination of the Pb isotope ratio was completed on a MAT-261 thermoelectric ion mass spectrometer. Lead isotopes were measured by using silica gel emitters and rhenium metal strips.

**Table 2.** Major and trace element and Sr-Nd-Pb isotopic compositions of Qiongduojiang gabbro in Tethys–Himalayan.

Sample	12FW58	12FW61	12FW63	13JT04	13JT05	13JT06	G1603H1	G1603H2	G1603H3	G1603H4
SiO <sub>2</sub>	43.92	46.37	42.25	42.66	44.49	44.56	47.81	47.91	47.22	48.02
TiO <sub>2</sub>	3.09	2.99	3.56	2.97	2.85	3.02	1.48	1.46	1.45	1.43
Al <sub>2</sub> O <sub>3</sub>	12.97	16.96	16.22	14.41	14.19	14.58	13.82	14.32	13.57	13.98
TFeO	11.42	9.92	11.11	9.98	8.35	8.76	13.28	12.7	12.54	12.6
MnO	0.19	0.13	0.13	0.15	0.13	0.13	0.17	0.16	0.17	0.17
MgO	9.70	4.03	6.61	7.03	7.36	7.34	7.56	6.97	7.04	6.85
CaO	8.50	6.25	6.77	7.78	11.09	10.79	9.38	9.36	10.07	9.70
Na <sub>2</sub> O	2.95	5.88	3.56	4.03	3.67	3.71	2.82	3.13	2.64	2.64
K <sub>2</sub> O	0.08	0.33	0.78	0.15	0.17	0.25	0.09	0.09	0.09	0.10
P <sub>2</sub> O <sub>5</sub>	0.61	0.72	0.42	0.49	0.35	0.44	0.13	0.14	0.13	0.15
LOI	6.21	6.59	8.65	9.26	5.92	4.93	3.39	3.72	5.06	4.31
Total	99.64	100.17	100.06	98.91	98.57	98.51	99.93	99.96	99.98	99.95
V	206.0	151.0	294.0	275.0	298.0	314.0	291.0	279.0	288.0	298.0
Cr	222.0	3.0	10.0	40.0	220.0	210.0	257.0	200.0	217.0	146.0
Co	47.0	27.0	48.0	36.0	35.0	38.0	52.9	49.5	51.6	53.6
Ni	172.0	9.0	45.0	45.0	69.0	73.0	58.2	54.3	55.5	49.7
Ga	21.0	22.0	20.0	20.0	18.0	19.0	21.0	20.4	20.3	21.7
Rb	4.2	12.0	28.0	3.6	4.3	6.2	1.3	0.9	1.0	1.1
Sr	582.0	697.0	389.0	635.0	843.0	592.0	323.0	353.0	337.0	358.0
Y	30.9	34.3	24.4	26.4	24.8	27.5	21.1	20.8	21.2	22.1
Zr	289.0	224.0	170.0	172.0	157.0	171.0	11.7	11.6	11.5	17.0
Nb	70.0	87.0	52.0	47.0	36.0	39.0	9.4	9.1	9.8	9.9
Cs	1.8	0.5	0.8	0.8	0.6	0.6	1.0	1.2	0.7	0.8
Ba	453.0	556.0	326.0	284.0	739.0	1450.0	6.6	6.2	5.4	7.0
La	43.3	41.1	25.8	27.2	21.8	25.0	8.2	8.0	8.0	8.6
Ce	87.2	81.0	49.7	55.6	45.2	51.5	17.1	16.5	17.0	17.8
Pr	10.8	9.9	6.2	6.8	5.7	6.3	2.4	2.3	2.3	2.5
Nd	43.1	39.7	25.0	29.5	25.4	29.6	11.4	10.8	11.2	11.7
Sm	9.1	8.9	5.8	6.6	6.0	7.0	3.1	3.0	3.0	3.2
Eu	3.0	2.7	2.0	2.4	2.2	2.5	1.1	1.1	1.0	1.1
Gd	8.1	8.2	5.6	6.8	6.5	7.3	3.2	3.2	3.3	3.5
Tb	1.2	1.2	0.9	1.0	1.0	1.1	0.7	0.7	0.7	0.7
Dy	6.2	6.7	4.8	5.5	5.4	5.8	4.0	4.1	4.2	4.3
Ho	1.1	1.3	0.9	1.0	1.0	1.0	0.8	0.8	0.8	0.8
Er	2.7	3.1	2.3	2.7	2.5	2.7	2.1	2.1	2.0	2.1
Tm	0.4	0.4	0.3	0.3	0.3	0.3	0.3	0.3	0.3	0.3
Yb	2.2	2.6	1.9	1.9	1.7	1.9	1.8	1.9	1.9	2.0
Lu	0.3	0.4	0.3	0.3	0.2	0.3	0.2	0.2	0.2	0.3
Hf	6.4	4.4	3.8	4.4	4.4	4.7	0.6	0.6	0.6	0.7
Ta	4.4	4.8	3.0	2.5	1.9	2.2	0.6	0.6	0.6	0.6
Pb	3.1	2.4	2.4	1.8	1.4	1.6	5.7	6.0	5.6	6.1
Th	5.9	5.7	3.8	3.5	2.8	3.2	0.7	0.7	0.7	0.8
U	1.5	1.3	0.9	0.9	0.7	0.8	0.1	0.1	0.1	0.1
<sup>87</sup> Sr/ <sup>86</sup> Sr	0.706739	0.706738	0.706719	0.707161	0.707302	0.707120	0.705702	0.705698	0.705661	0.705749
2SE	0.000014	0.000013	0.000014	0.000013	0.000014	0.000014	0.000016	0.000013	0.000014	0.000016
<sup>87</sup> Sr/ <sup>86</sup> Sr(t)	0.706726	0.706705	0.706584	0.707151	0.707293	0.707101	0.705696	0.705508	0.705656	0.705744
<sup>143</sup> Nd/ <sup>144</sup> Nd	0.512878	0.512896	0.512917	0.512918	0.512935	0.512937	0.512808	0.513133	0.512795	0.512801
2SE	0.000003	0.000004	0.000004	0.000004	0.000003	0.000004	0.000007	0.000014	0.000012	0.000011
ε <sub>Nd</sub> (0)	4.7	5.0	5.4	5.5	5.8	5.8	3.3	9.7	3.1	3.2
ε <sub>Nd</sub> (t)	5.1	5.4	5.8	5.8	6.1	6.1	3.5	9.8	3.2	3.3
f <sub>Sm</sub> /Nd	−0.35	−0.31	−0.29	−0.31	−0.27	−0.28	−0.20	−0.19	−0.2	−0.2
( <sup>206</sup> Pb/ <sup>204</sup> Pb) <sub>t</sub>							18.52	18.52	18.53	18.52
( <sup>207</sup> Pb/ <sup>204</sup> Pb) <sub>t</sub>							15.64	15.65	15.65	15.65
( <sup>208</sup> Pb/ <sup>204</sup> Pb) <sub>t</sub>							38.99	39.00	39.03	38.99

Note: 12FW58–13JT06 Date from [30]; LOI: loss on ignition.

#### 4. Results

The CL image shows that zircon from the Qiongduojiang gabbro has obvious oscillatory zoning characteristics, indicating the origin of magmatic zircon. Most zircons are about 100–150 μm long with length–width ratios of 1:1–2:1. The <sup>206</sup>Pb/<sup>238</sup>U age results of 27 zircons are listed in Table 1, ranging from 48.0 to 2852.6 Ma, in which 7 zircons have the weighted average age of 46.1 ± 1.7 Ma (MSWD = 0.81) (Figure 3), and their Th/U ratios are between 0.9 and 6.7 (Table 1), which indicates that they are typical magmatic zircons [42]. Therefore, this weighted-average age can represent the crystallization age of the Qiongduojiang gabbro.

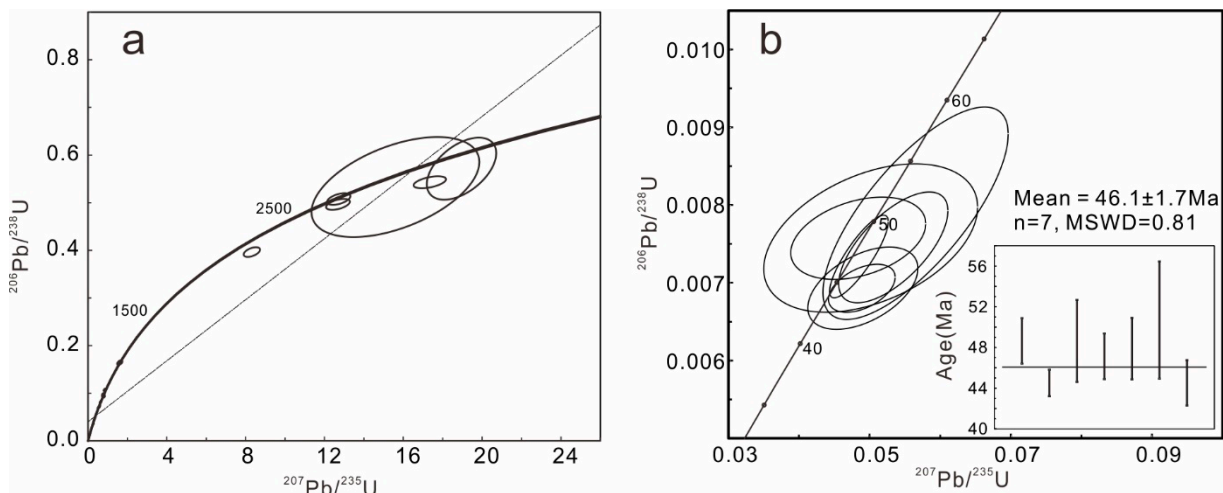


**Figure 3.**  $^{207}\text{Pb}/^{235}\text{U}$  vs.  $^{206}\text{Pb}/^{238}\text{U}$  ratios of all analyzed zircons (a) and zircons with Concordia ages (b) for the Qiongduojiang gabbro in Tethys–Himalayan.

The results of whole-rock major and trace elements and Rb–Sr, Sm–Nd, and Pb isotopes of Qiongduojiang gabbro are listed in Table 2. For comparison, the data of Langshan gabbro published by [30] are also listed in Table 2. The analysis results show that the  $\text{SiO}_2$  content of Qiongduojiang gabbro is 47.2–48.0 wt.%, the  $\text{TiO}_2$  content is 1.4–1.5 wt.%, and the MgO content is 6.9–7.6 wt.% (Figure 4). The calculated  $\text{Mg}^\#$  value ( $\text{Mg}\text{-number} = \text{Mg}/(\text{Mg} + \text{Fe})$ , in molecular) is 49.5–50.6. The Qiongduojiang gabbro is characterized by high Ni and Cr contents (49.7–58.2 ppm and 146–257 ppm, respectively), high light rare earth elements, and low heavy rare earth elements ( $\text{La}_\text{N}/\text{Yb}_\text{N} = 5.1\text{--}5.5$ ), which is similar to E-MORB (Figure 5a). In the primitive-mantle-normalized spider diagram (Figure 5b), the Qiongduojiang gabbro is rich in Nb and Ta and is characterized by a loss of large ion lithophile elements (i.e., Rb and Ba). The trace element characteristics of Qiongduojiang gabbro are obviously different from Gangdese arc magmatic rocks but are close to typical E-MORB basic rocks (Figure 5b). The above geochemical characteristics are different from the geochemical composition of Eocene basic magmatic rocks in Langshan, Tethys Himalayan belt, which have been reported by [30]. The Langshan gabbro shows high Ti ( $\text{TiO}_2 = 3.08\text{--}3.89$  wt.%) and high  $\text{La}_\text{N}/\text{Yb}_\text{N}$  (15.8–24.6) ratios with typical OIB characteristics.

The calculated  $^{87}\text{Sr}/^{86}\text{Sr}(t)$  isotope ratio of Qiongduojiang gabbro is 0.705508–0.705744. The value of  $^{143}\text{Nd}/^{144}\text{Nd}$  is 0.512795–0.513133, with a calculated  $\epsilon_{\text{Nd}}(t)$  value of 3.2–9.8. The initial  $^{206}\text{Pb}/^{204}\text{Pb}$ ,  $^{207}\text{Pb}/^{204}\text{Pb}$ , and  $^{208}\text{Pb}/^{204}\text{Pb}$  ratios corrected by crystallization age are 18.52–18.53, 15.64–15.65, and 38.99–39.03, respectively. It shows the characteristics of high radiogenic Pb isotopic composition.

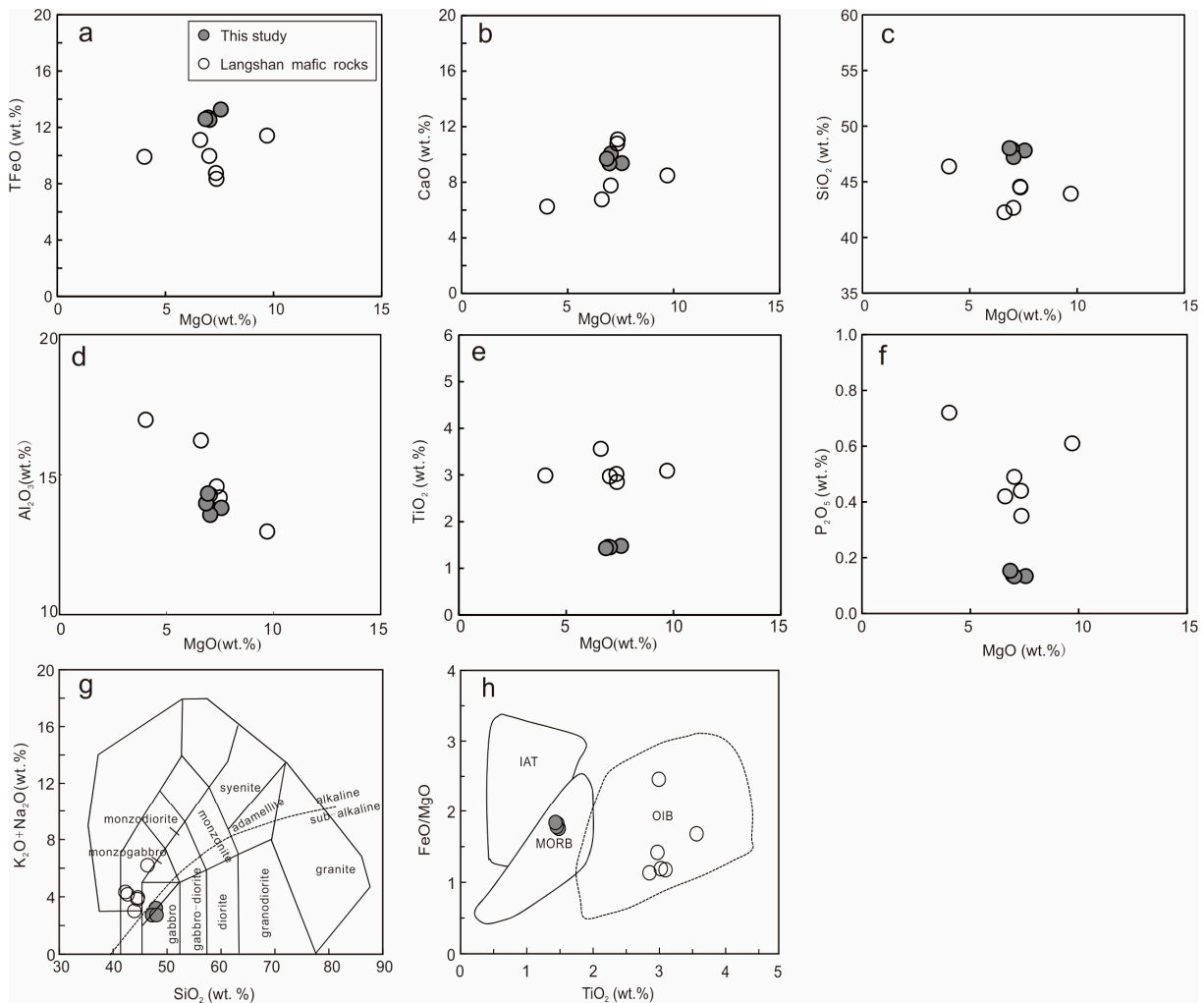


**Figure 4.** (a) MgO vs. TFeO; (b) MgO vs. CaO; (c) MgO vs. SiO<sub>2</sub>; (d) MgO vs. Al<sub>2</sub>O<sub>3</sub>; (e) MgO vs. TiO<sub>2</sub>; (f) MgO vs. P<sub>2</sub>O<sub>5</sub>; (g) SiO<sub>2</sub> vs K<sub>2</sub>O+Na<sub>2</sub>O [43]; and (h) TiO<sub>2</sub> vs. FeO/MgO [44] of the Qiongduojiang gabbro.

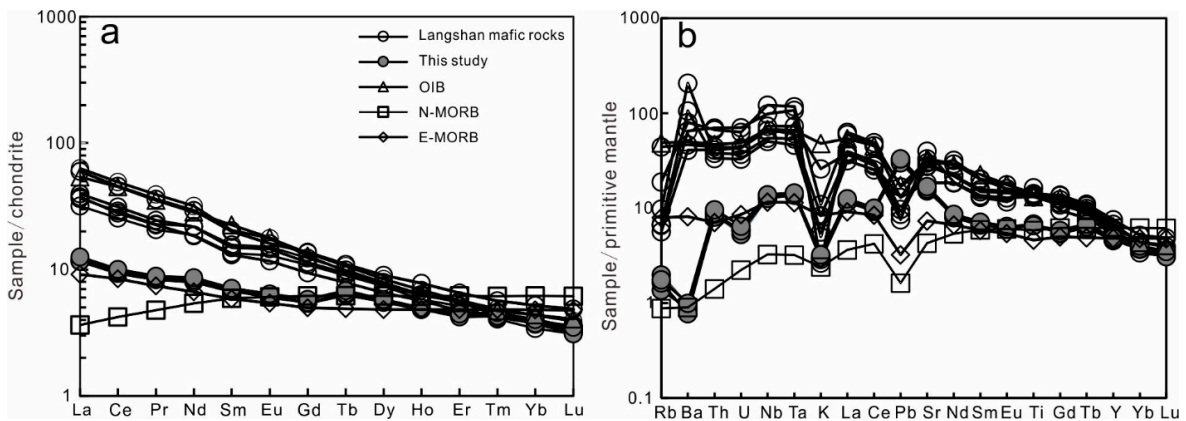


**Figure 5.** (a) Chondrite-normalized rare earth element (REE) patterns and (b) primitive-mantle-normalized spider diagrams of the Qiongduojiang gabbro; OIB, N-MORB, E-MORB, Chondrite, and primitive-mantle-normalization standard values are from [45]. Data of Langshan mafic rocks from [30].

## 5. Discussion

### 5.1. Geochronology of the Qiongduojiang Gabbro and Coeval Magmatism along YTSZ

The newly obtained zircon U-Pb age of the Qiongduojiang gabbro was ca. 46 Ma. On the north side of YTSZ, coeval magmatism is represented mainly by Linzizong volcanic rocks and their intrusive counterparts [8,15–17,21,46]. The Linzizong volcanic successions consist of Dianzhong and Nianbo formations (69–50 Ma), as well as the Pana Formation (50–43 Ma). They are all characterized by the enrichment of LILE and depletion of HFSE. Fairly intense magmatic activities occurred at ca. 50 Ma, and heterogeneous intrusive rocks were derived from the asthenospheric mantle, mantle wedge, metasomatized lithospheric mantle, basaltic lower crust, and basement of the Lhasa terrane [16]. For example, in the Quxu batholith, Ma et al. [47] reported ca. 48 Ma Napuri adakitic rocks formed by lower crustal melting, whereas Wang et al. [48] obtained ages of ca. 51 Ma for the gabbro-norites, quartz diorites, and tonalites, which are derived from mixing of the asthenospheric mantle and juvenile lower crust. Zhou et al. [12] summarized that during ca. 53–49 Ma, the Linzizong volcanic rocks and coeval plutons have comparable compositions to arc rocks but show significant input of asthenospheric mantle with  $\epsilon\text{Nd}_{(t)}$  values up to +9.8 and zircon  $\epsilon\text{Hf}_{(t)}$  values up to +15.1 [8,15]. In the Yangbajiang area, the ~50 Ma shoshonitic and ultrapotassic rocks are related to a mantle source previously metasomatized by fluids from the oceanic crust and later re-fertilized by sediment-derived melts [49]. Wang et al. [50] identified two episodes of Eocene mafic magmatism in the Quxu area; the early suite of gabbro (ca. 53 Ma) shows typical arc features and was derived from partial melting of lithospheric mantle metasomatized by fluids. However, the later suite of hornblende gabbro (ca. 48 Ma) has mixture characteristics of the asthenospheric mantle and enriched lithospheric mantle metasomatized by subducted sediment melts. These mafic rocks may indicate that in the southern Lhasa terrane, mafic magmatic “flare-up” events progressively propagated eastward from 56 to 50 Ma. Zhou et al. [12] summarized that during the 53–49 Ma, the most voluminous magmatism in the Gangdese belt shows a thermal anomaly (up to 980 °C, Ti-in-zircon temperature), which is attributed to asthenospheric mantle upwelling. Shu et al. [51] supported this conclusion with their work on the Ringqênzê plutonic complex.

On the south side of YTSZ, Pullen et al. [18] reported a zircon U-Pb age of 43.9 Ma for a granite pluton in the Xiao Gurla Range. Ding [49] found that an undeformed leucogranite that intrudes into pelitic schist in the core of the Niuku anticline has a crystallization age of ca. 45 Ma and is a result of crustal anatexis and exhumation in the northern Tethys. Strongly deformed porphyritic two-mica granite gneiss dykes at the Ramba dome were derived mainly from the partial melting of mafic material in the lower crust at ca. 44 Ma [52]. The Dala and Quedang granites near the Yalaxiangbo dome were found to have zircon U-Pb ages ranging from 46 to 44 Ma [53]. Ji et al. [30] identified the Langshan gabbro with a titanite U-Pb age of ca. 45 Ma as the first evidence for partial melting of the asthenosphere in the Ramba dome area. Zeng et al. [19] suggested that the ca. 44–42 Ma high Sr/Y granitic rocks in the Yardoi dome, Dala, and Quetang areas were due to the partial melting of the amphibolite dominant source. These granites are related to crustal thickening and led to the formation of high-density eclogitic rocks beneath the Tethyan Himalaya.

In general, during ca. 45–50 Ma, voluminous volcanic rocks and their intrusive counterparts were distributed on both sides of YTSZ, representing intense tectono-magmatic activities that occurred during the Eocene in this area. Significant mantle contributions (material and heat) evolved during this magmatic flare-up.

### 5.2. Characteristics of Magma Sources

Before using the whole-rock geochemical data for discussion, the impact of hydrothermal alteration on elements, especially easily migrated elements, must be evaluated. The whole-rock loss on ignition (LOI) of Qiongduojiang gabbro ranges from 3.39 wt% to 5.06 wt%, indicating that these samples were altered to some degree. This may explain the decoupling of the Sr and Nd isotopic composition of the Qiongduojiang gabbro, since

Sr is more easily modified by alteration. However, the LOI does not correlate with major elements or mobile trace elements (K, Rb, Sr, and Ba) (not shown). Our petrography study shows that in the Qiongduojiang gabbro samples, the later hydrothermal alteration is mainly filled carbonate veinlets, rather than the metasomatic alteration of feldspar and ferromagnetic minerals. Therefore, the influence of hydrothermal alteration on the whole-rock geochemical data is very limited.

During the upward migration of mafic magmas, crustal contamination might inevitably occur, and its geochemical composition will gradually evolve into the crustal composition. Inherited zircons in the Qiongduojiang gabbro (Table 1) indicate that crustal contamination also occurred. The degree of crustal contamination can be judged by using the geochemical indexes of different elements of the crust and mantle. For example, the radius of U ions is large and tends to be enriched in the crust, Nb is a typical lithophile element, and their different element behaviors in the crust (Nb/U ratio) can be used as an indicator of the degree of crustal contamination. In addition, with the increase in the degree of crustal contamination, the isotopic ratio of basic magma will evolve towards the crust. Therefore, the degree of contamination can also be judged by using SiO<sub>2</sub> and Nd homotopy mapping. The Qiongduojiang gabbro shows high Nb/U ratios (72–84) and Nb/La ratios greater than 1. These data do not indicate obvious crustal contamination. On the other hand, the SiO<sub>2</sub> and ε<sub>Nd</sub>(t) isotopes of Qiongduojiang gabbro do not show negative correlations, indicating that the crustal contamination degree of the Qiongduojiang gabbro is not significant.

The major and trace element composition of the Qiongduojiang gabbro shows a typical MORB-like characteristic. For example, it is characterized by a lower TiO<sub>2</sub> content (1.43 to 1.48 wt.%) than the oceanic island basalt and a low TFeO/MgO ratio (1.76 to 1.84) (Figure 4h; [44]). The V content of the Qiongduojiang gabbro ranges from 279 to 298 ppm with Ti/V ratios between 20 and 50 [54]. Both the REE distribution pattern and primitive-mantle-normalized spider diagram of the Qiongduojiang gabbro are broadly parallel to the enriched MORB (E-MORB), with lower Rb and Ba contents. In the Ta/Yb versus Th/Yb diagram (Figure 6a; [55]), all the Qiongduojiang gabbro plots are in the MORB-OIB array and close to the E-MORB. Since basalt with a large crustal component plots mainly above the MORB-OIB array due to the selective addition of Th, crustal contamination in Qiongduojiang gabbro is negligible. The Nb/Yb ratio of Qiongduojiang gabbro is higher than 1.45, and the TiO<sub>2</sub>/Yb ratio is lower than OIB, indicating shallower melting than OIB (Figure 6b; [55]). Hawkesworth et al. [56] suggested that mantle metasomatized by subduction-related fluids contains high Ba, whereas mantle with slab components with high Th contents. The Qiongduojiang gabbro has a Th/Nb of 0.076 to 0.083 and a Ba/Th of 7.34 to 8.95, which is close to the E-MORB composition without visible fluid/melt-related enrichment [50].

The Qiongduojiang gabbro has <sup>87</sup>Sr/<sup>86</sup>Sr<sub>(t)</sub> ratios of 0.7055 to 0.7057 and Nd isotope (ε<sub>Nd</sub>(t) values of 3.2–9.8) (Figure 6c), which are similar to Neo-Tethyan ophiolite [57–60]. The <sup>206</sup>Pb/<sup>204</sup>Pb<sub>(t)</sub>, <sup>207</sup>Pb/<sup>204</sup>Pb<sub>(t)</sub>, and <sup>208</sup>Pb/<sup>204</sup>Pb<sub>(t)</sub> ratios of Qiongduojiang gabbro are approximately 18.52, 15.65, and 39.00, respectively. These lead isotopic compositions are consistent with those of Eocene mafic rock and shoshonite in south Tibet, which have been interpreted as the products of enriched mantle [61]. In summary, both the major and trace elements, as well as Sr-Nd-Pb isotopic compositions of the Qiongduojiang gabbro, indicate that it was derived from an enriched mantle source. Similar E-MORB-like basaltic lavas have also been reported in the Purang massif in the Tethys Himalaya [62]. In the Yalaxiangbo area, these E-MORB-like magmas are products of the N-MORB mantle mixed with OIB-like magmas [63].

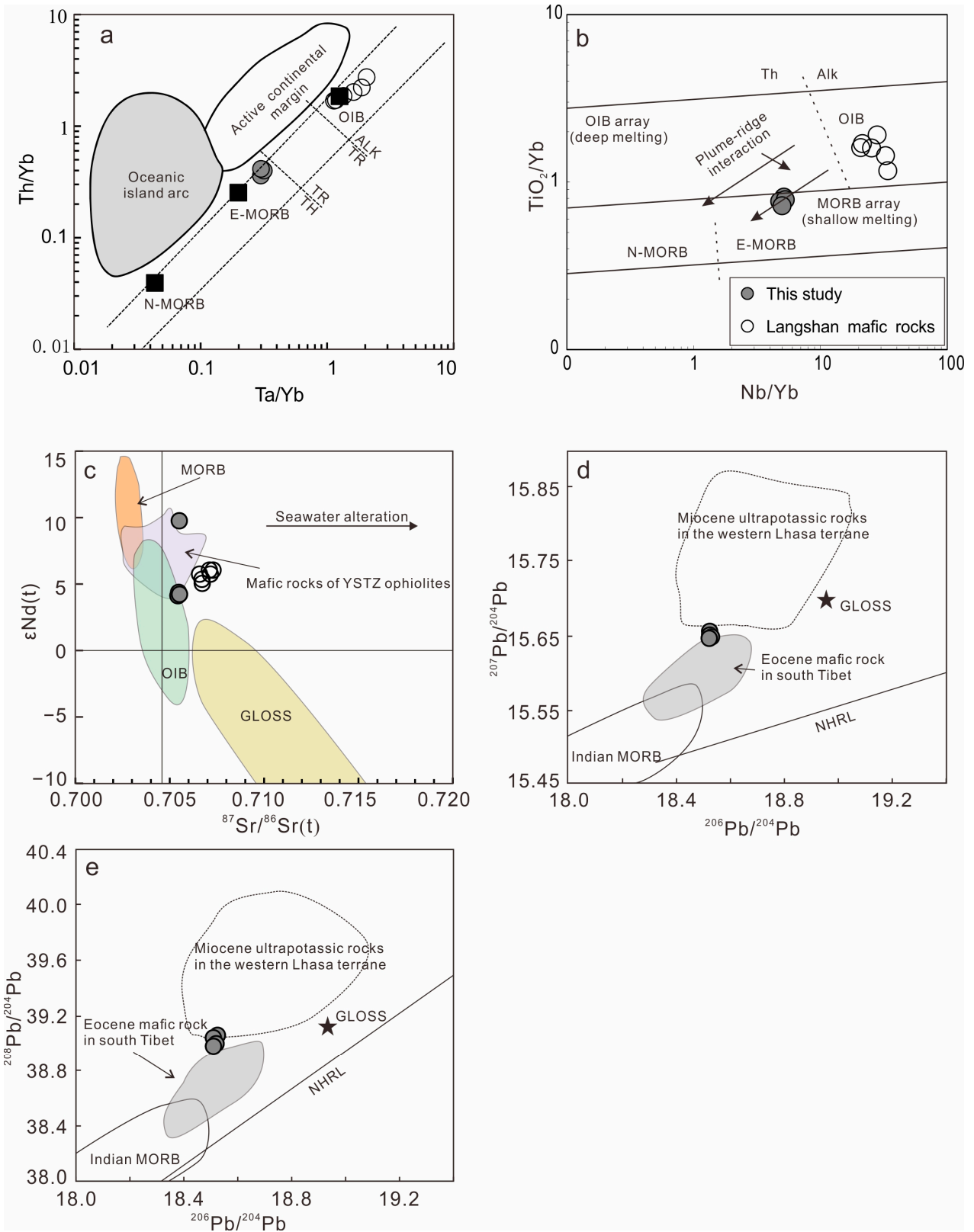


**Figure 6.** (a) Ta/Yb vs. Th/Yb and (b) Nb/Yb vs. TiO<sub>2</sub>/Yb diagrams [55]; (c) <sup>87</sup>Sr/<sup>86</sup>Sr(t) vs. εNd(t) diagram [56]; (d) <sup>206</sup>Pb/<sup>204</sup>Pb vs. <sup>207</sup>Pb/<sup>204</sup>Pb; (e) <sup>206</sup>Pb/<sup>204</sup>Pb vs. <sup>208</sup>Pb/<sup>204</sup>Pb (modified after [61]).

### 5.3. Tectonic Setting

Guillot et al. [64] noticed temperature increases during the retrogressive evolution of the Tso Moriri eclogites in the northwest Himalayas. Extensively crustal melting formed the magmatic flare-up in the southern Lhasa block (ca. 55–45 Ma) [15,17], OIB-type gabbro in the Tethys [30], and Mid-Eocene granites in the northern Himalayan Gneiss Domes [19]. Studies about the Cenozoic convergence rate between India and Eurasia show two significant decelerations [65–67]. The second deceleration is due to the Neo-Tethyan oceanic slab breakoff, which lost the slab pull at ca. 45 Ma. Consequently, the speed decreased from 8–10 cm/yr to 4–6 cm/yr and remained nearly constant rate after that [66,67].

In the early Eocene, major topographic uplift was identified in southern Tibet. Large volumes of early Eocene sediments were deposited in the Bangladesh basin [68]. The ultra-high pressure (UHP) rocks from the Western Himalayas were reported with ages ca. 45–55 Ma [20]. The UHP eclogite in the Kaghan Valley recorded a very rapid exhumation rate from ~100 to ~35 km during ca. 46 to 44 Ma [69]. Based on paleomagnetic reconstructions and tomographical characters, Negredo et al. [70] suggested that the Indian slab breakoff occurred at ca. 44–48 Ma after the initial Indian–Eurasian continental collision.

The evidence mentioned above includes asthenosphere upwelling, crustal uplift, and deceleration of convergence between the Indian and Eurasian plates all supporting a slab breakoff that happened in South Tibet during the middle Eocene (Figure 7). The ca. 46 Ma Qionduojiang gabbro was formed during the slab breakoff. Upwelling asthenosphere offered the heat to partially melt the lithospheric mantle metasomatized by OIB-like components in the Yalaxiangbo area [71].

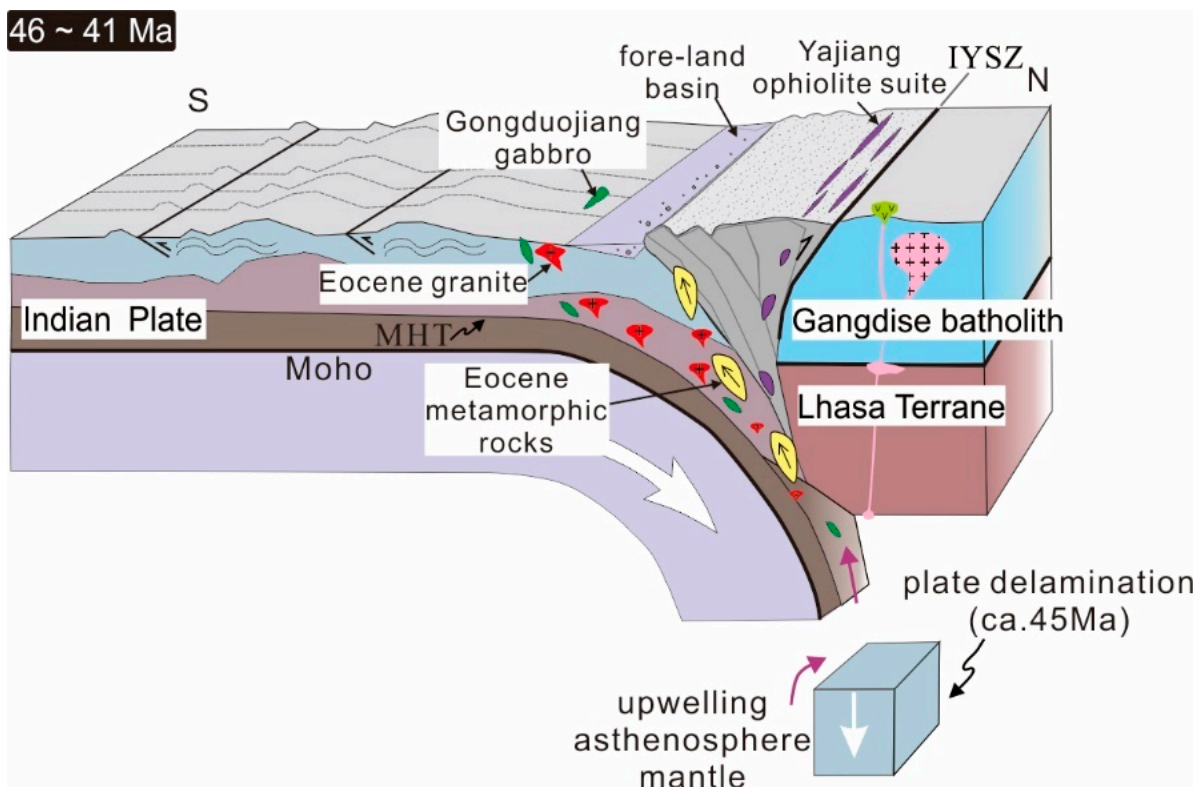


**Figure 7.** Tectonic setting of Qionduojiang gabbro in south Tibet (modified after [30]).

### 5.4. Implication of Metallogenesis

The Eocene Neo-Tethyan oceanic slab breakoff triggered the asthenosphere upwelling and contributed to the modification, remelting, and mixing of the upper continental crustal materials to form fertile porphyritic intrusions and associated mineralization. Similar to the Yulong porphyry copper belt, ore-related porphyries were formed by partial melting of

phlogopite-bearing amphibolite or amphibolite eclogite and are related to the enrichment mantle, which was altered by older subducted slab-derived fluid [72]. In the Gangdese belt, Zhao et al. [73] used a Nd-Hf isotopic mixing model to reveal a higher influx of mantle material into the fertile magma source during this interval and related ore deposits [74–76].

The Gangdese porphyry copper deposits are generally associated with the Miocene calc-alkaline to high-K calc-alkaline granitoids, which have similar isotopic composition and inherited ages to those of Paleocene–Eocene arc rocks, indicating that the lower crust source of the metallogenic Miocene magmas is composed predominantly of the Paleocene–Eocene arc rocks [76,77]. During the Paleocene–Eocene slab rollback and slab breakoff processes, the chalcophile (such as Cu) and siderophile metals (such as Mo and Au) were left as residues in deep crustal arc cumulate zones and/or metasomatized mantle lithosphere, rendering the subduction-modified Tibetan lithosphere fertile [78]. This conclusion is supported by the recently discovered Paleocene–Eocene lower crustal hornblendite, which has sulfides with high Cu contents of up to 1000 ppm [79]. Thus, the Qiongduojiang gabbro represents the Eocene upwelling asthenosphere playing a vital role in the formation of porphyry copper deposits in Tibet.

## 6. Conclusions

- (1) The crystallization age of the Qiongduojiang gabbro is constrained to  $46.1 \pm 1.7$  Ma, representing large-scale asthenosphere upwelling during the middle Eocene.
- (2) Unlike the coeval Langshan gabbro, the Qiongduojiang gabbro shows typical E-MORB-like characteristics, indicating the heterogeneous composition of the mantle. The Qiongduojiang gabbro is direct evidence of slab breakoff, which induced linear magmatic activities along the YTSZ, the convergence deceleration of Indian and Eurasian plates, and the uplift of ultrahigh-pressure rocks.
- (3) Eocene upwelling asthenosphere played a critical role in the Cu pre-enrichment in the Gangdese arc root and the consequent formation of the Miocene porphyry Cu deposits.

**Author Contributions:** Conceptualization, J.L. and Y.H.; methodology, Q.W.; software, L.Z.; validation, T.X. and B.W.; formal analysis, Z.L.; investigation, Z.L.; resources, H.C.; data curation, W.L. and Z.D.; writing—original draft preparation, J.L. and Y.H.; writing—review and editing, J.L. and Y.H.; visualization, L.Z.; supervision, Y.H.; project administration, Y.H.; funding acquisition, Y.H. All authors have read and agreed to the published version of the manuscript.

**Funding:** This research was funded by the Geological Survey project, grant number ZD20220310, DD20220971, and the National Key R&D Program of China, grant number 2018YFC0604100.

**Data Availability Statement:** Not applicable.

**Acknowledgments:** We sincerely thank the Qinghai–Tibet Plateau Geology and Prospecting Innovation Team of the Chengdu Center of China Geological Survey for their help in the field. We would like to thank engineers Jincheng Zhang, Bozhi Gong, and Liu Lu for their participation in the field investigation.

**Conflicts of Interest:** The authors declare no conflict of interest.

## References

1. Ma, X.X.; Meert, J.G.; Xu, Z.Q.; Zhao, Z.B. Evidence of magma mixing identified in the Early Eocene Caina pluton from the Gangdese Batholith, southern Tibet. *Lithos* **2017**, *278–281*, 126–139. [[CrossRef](#)]
2. Meng, Y.K.; Xu, Z.Q.; Santosh, M.; Ma, X.X.; Chen, X.J.; Guo, G.L.; Liu, F. Late Triassic crustal growth in southern Tibet: Evidence from the Gangdese magmatic belt. *Gondwana Res.* **2016**, *37*, 449–464. [[CrossRef](#)]
3. Wang, C.; Ding, L.; Zhang, L.Y.; Kapp, P.; Pullen, A.; Yue, Y.H. Petrogenesis of Middle–Late Triassic volcanic rocks from the Gangdese belt, southern Lhasa terrane: Implications for early subduction of Neo-Tethyan oceanic lithosphere. *Lithos* **2016**, *262*, 320–333. [[CrossRef](#)]
4. Kang, Z.Q.; Xu, J.F.; Wilde, S.A.; Feng, Z.H.; Chen, J.L.; Wang, B.D.; Fu, W.C.; Pan, H.B. Geochronology and geochemistry of the Sangri Group Volcanic Rocks, Southern Lhasa Terrane: Implications for the early subduction history of the Neo-Tethys and Gangdese Magmatic Arc. *Lithos* **2014**, *200–201*, 157–168. [[CrossRef](#)]

5. Ji, W.Q.; Wu, F.Y.; Chung, S.L.; Li, J.X.; Liu, C.Z. Zircon U-Pb geochronology and Hf isotopic constraints on petrogenesis of the Gangdese batholith, southern Tibet. *Chem. Geol.* **2009**, *262*, 229–245. [[CrossRef](#)]
6. Chu, M.F.; Chung, S.L.; Song, B.; Liu, D.Y.; O'Reilly, S.Y.; Pearson, N.J.; Ji, J.Q.; Wen, D.J. Zircon U-Pb and Hf isotope constraints on the Mesozoic tectonics and crustal evolution of southern Tibet. *Geology* **2006**, *34*, 745–748. [[CrossRef](#)]
7. Hu, X.M.; Garzanti, E.; Wang, J.G.; Huang, W.T.; An, W.; Webb, A. The timing of India-Asia collision onset—Facts, theories, controversies. *Earth Sci. Rev.* **2016**, *160*, 264–299. [[CrossRef](#)]
8. Wang, R.; Richards, J.P.; Hou, Z.Q.; An, F.; Creaser, R.A. Zircon U-Pb age and Sr-Nd-Hf-O isotope geochemistry of the Paleocene–Eocene igneous rocks in western Gangdese: Evidence for the timing of Neo-Tethyan slab breakoff. *Lithos* **2015**, *224–225*, 179–194. [[CrossRef](#)]
9. Wang, R.; Richards, J.P.; Zhou, L.M.; Hou, Z.Q.; Stern, R.A.; Creaser, R.A.; Zhu, J.J. The role of Indian and Tibetan lithosphere in spatial distribution of Cenozoic magmatism and porphyry Cu-Mo ± Au deposits in the Gangdese belt, southern Tibet. *Earth Sci. Rev.* **2015**, *150*, 68–94. [[CrossRef](#)]
10. Gao, Y.F.; Wei, R.H.; Hou, Z.Q.; Tian, S.H.; Zhao, R.S. Eocene high-MgO volcanism in southern Tibet: New constraints for mantle source characteristics and deep process. *Lithos* **2008**, *105*, 63–72. [[CrossRef](#)]
11. van der Voo, R.; Spakman, W.; Bijwaard, H. Tethyan subducted slabs under India. *Earth Planet. Sci. Lett.* **1999**, *171*, 7–20. [[CrossRef](#)]
12. Zhou, L.M.; Wang, R.; Hou, Z.Q.; Li, C.; Zhao, H.; Li, X.W.; Qu, W.J. Hot Paleocene-Eocene Gangdese arc: Growth of continental crust in southern Tibet. *Gondwana Res.* **2018**, *62*, 178–197. [[CrossRef](#)]
13. Shui, X.F.; Klemd, R.; He, Z.Y.; Mao, J.W.; Zhao, Y.Y. Geochronology and petrogenesis of Eocene gabbros and granitic rocks of the eastern Gangdese belt, southern Tibet: Implications for the timing of India-Asia collision. *Gondwana Res.* **2021**, *97*, 145–157. [[CrossRef](#)]
14. Hou, Z.Q.; Zheng, Y.C.; Lu, Z.W.; Xu, B.; Wang, C.M.; Zhang, H.R. Growth, thickening and Evolution of the thickened crust of the Tibet Plateau. *Acta Geol. Sin.* **2020**, *94*, 2797–2815, (In Chinese with English abstract).
15. Zhu, D.C.; Wang, Q.; Zhao, Z.D.; Chung, S.L.; Cawood, P.A.; Niu, Y.L.; Liu, S.A.; Wu, F.Y.; Mo, X.X. Magmatic record of India-Asia collision. *Sci. Rep.* **2015**, *5*, 14289. [[CrossRef](#)] [[PubMed](#)]
16. Lee, H.Y.; Chung, S.L.; Ji, J.Q.; Qian, Q.; Gallet, S.; Lo, C.H.; Lee, T.Y.; Zhang, Q. Geochemical and Sr–Nd isotopic constraints on the genesis of the Cenozoic Linzizong volcanic successions, southern Tibet. *J. Asian Earth Sci.* **2012**, *53*, 96–114. [[CrossRef](#)]
17. Lee, H.Y.; Chung, S.L.; Lo, C.H.; Ji, J.Q.; Lee, T.Y.; Qian, Q.; Zhang, Q. Eocene Neotethyan slab breakoff in southern Tibet inferred from the Linzizong volcanic record. *Tectonophysics* **2009**, *477*, 20–35. [[CrossRef](#)]
18. Pullen, A.; Kapp, P.; DeCelles, P.G.; Gehrels, G.E.; Ding, L. Cenozoic anatexis and exhumation of Tethyan Sequence rocks in the Xiao Gurla Range, Southwest Tibet. *Tectonophysics* **2011**, *501*, 28–40. [[CrossRef](#)]
19. Zeng, L.S.; Gao, L.E.; Xie, K.J.; Zeng, J.L. Mid-Eocene high Sr/Y granites in the Northern Himalayan Gneiss Domes: Melting thickened lower continental crust. *Earth Planet. Sci. Lett.* **2011**, *303*, 251–266. [[CrossRef](#)]
20. Kohn, M.J.; Parkinson, C.D. Petrologic case for Eocene slab breakoff during the Indo-Asian collision. *Geology* **2002**, *30*, 591–594. [[CrossRef](#)]
21. Chung, S.L.; Chu, M.F.; Zhang, Y.Q.; Xie, Y.W.; Lo, C.H.; Lee, T.Y.; Lan, C.Y.; Li, X.H.; Zhang, Q.; Wang, Y.Z. Tibetan tectonic evolution inferred from spatial and temporal variations in post-collisional magmatism. *Earth Sci. Rev.* **2005**, *68*, 173–196. [[CrossRef](#)]
22. Xu, Y.G.; Lan, J.B.; Yang, Q.J.; Huang, X.L.; Qiu, H.N. Eocene break-off of the NeoTethyan slab as inferred from intraplate-type mafic dykes in the Gaoligong orogenic belt, eastern Tibet. *Chem. Geol.* **2008**, *255*, 439–453. [[CrossRef](#)]
23. Davies, J.H.; von Blanckenburg, F. Slab breakoff: A model of lithosphere detachment and its test in the magmatism and deformation of collisional orogens. *Earth Planet. Sci. Lett.* **1995**, *129*, 85–102. [[CrossRef](#)]
24. von Blanckenburg, F.; Davies, J.H. Slab breakoff: A model for syncollisional magmatism and tectonics in the Alps. *Tectonics* **1995**, *14*, 120–131. [[CrossRef](#)]
25. Garzanti, E.; Radeff, G.; Malusà, M.G. Slab breakoff: A critical appraisal of a geological theory as applied in space and time. *Earth Sci. Rev.* **2018**, *177*, 303–319. [[CrossRef](#)]
26. Liou, J.G.; Zhang, R.Y.; Ernst, W.G.; Iii, R.D.; Maruyama, S. High-pressure minerals from deeply subducted metamorphic rocks. *Rev. Mineral. Geochem.* **1998**, *37*, 33–96.
27. England, P.; Molnar, P. Surface uplift, uplift of rocks, and exhumation of rocks. *Geology* **1990**, *18*, 1173–1177. [[CrossRef](#)]
28. Niu, Y.L. Slab break-off: A causal mechanism or pure convenience. *Sci. Bull.* **2017**, *62*, 456–461. [[CrossRef](#)]
29. Freeburn, R.; Bouilhol, P.; Maunder, B.; Magni, V.; van Hunen, J. Numerical models of the magmatic processes induced by slab break-off. *Earth Planet. Sci. Lett.* **2017**, *478*, 203–213. [[CrossRef](#)]
30. Ji, W.Q.; Wu, F.Y.; Chung, S.L.; Wang, X.C.; Liu, C.Z.; Li, Q.L.; Liu, Z.C.; Liu, X.C.; Wang, J.G. Eocene Neo-Tethyan slab breakoff constrained by 45 Ma oceanic island basalt-type magmatism in southern Tibet. *Geology* **2016**, *44*, 283–286. [[CrossRef](#)]
31. Yin, A.; Harrison, T. Geologic evolution of the Himalayan–Tibetan orogen. *Annu. Rev. Earth Planet. Sci.* **2000**, *28*, 211–280. [[CrossRef](#)]
32. Hu, X.M.; Jansa, L.; Wang, C.S. Upper Jurassic–Lower Cretaceous stratigraphy in south-eastern Tibet. A comparison with the western Himalayas. *Cretac. Res.* **2008**, *29*, 301–315. [[CrossRef](#)]

33. Liu, G.; Einsele, G. Jurassic sedimentary facies and paleogeography of the former Indian passive margin in southern Tibet. In *Himalaya and Tibet: Mountain Roots to Mountain Tops*; MacFarlane, A., Sorkhabi, R.B., Quade, J., Eds.; Geological Society of America: Boulder, CO, USA, 1999; Volume 328, pp. 75–108.
34. Hu, X.M.; Sinclair, H.D.; Wang, J.G.; Jiang, H.H.; Wu, F.Y. Late Cretaceous–Palaeogene stratigraphic and basin evolution in the Zhepure Mountain of southern Tibet: Implications for the timing of India–Asia initial collision. *Basin Res.* **2012**, *24*, 520–543. [[CrossRef](#)]
35. Ratschbacher, L.; Frisch, W.; Liu, G.H.; Chen, C.S. Distributed deformation in southern and western Tibet during and after the India–Asia collision. *J. Geophys. Res. Solid Earth* **1994**, *99*, 19917–19945. [[CrossRef](#)]
36. Li, X.; Wang, C.; Hu, X. Stratigraphy of deep-water Cretaceous deposits in Gyangze, southern Tibet, China. *Cretac. Res.* **2005**, *26*, 33–41. [[CrossRef](#)]
37. Zhang, Z.M.; Dong, X.; Santosh, M.; Liu, F.; Wang, W.; Yiu, F.; He, Z.Y.; Shen, K. Petrology and geochronology of the Namche Barwa Complex in the eastern Himalayan syntaxis, Tibet: Constraints on the origin and evolution of the north-eastern margin of the Indian Craton. *Gondwana Res.* **2012**, *21*, 123–137. [[CrossRef](#)]
38. Zeng, L.S.; Liu, J.; Gao, L.E.; Xie, K.J.; Wen, L. Early Oligocene crustal anatexis in the Yardoi gneiss dome, southern Tibet and geological implications. *Chin. Sci. Bull.* **2009**, *54*, 104–112. [[CrossRef](#)]
39. Zeng, L.S.; Gao, L.E.; Tang, S.H.; Hou, K.J.; Guo, C.L.; Hu, G.Y. Eocene magmatism in the Tethyan Himalaya, southern Tibet. *Geol. Soc. Lond. Spec. Publ.* **2015**, *412*, 287–316. [[CrossRef](#)]
40. Liu, Y.S.; Hu, Z.C.; Gao, S.; Günther, D.; Xu, J.; Gao, C.G.; Chen, H.H. In situ analysis of major and trace elements of anhydrous minerals by LA-ICP-MS without applying an internal standard. *Chem. Geol.* **2008**, *257*, 34–43. [[CrossRef](#)]
41. Ludwig, K.R. *User's Manual for Isoplot/Ex, Version 3.0: S Geochronological Toolkit for Microsoft Excel*; Berkeley Geochronology Center Special Publication: Berkeley, CA, USA, 2003.
42. Hoskin, P.W.; Ireland, T.R. Rare earth element chemistry of zircon and its use as a provenance indicator. *Geology* **2000**, *28*, 627–630. [[CrossRef](#)]
43. Middlemost, E.A. Naming materials in the magma/igneous rock system. *Earth-Sci. Rev.* **1994**, *37*, 215–224. [[CrossRef](#)]
44. Glassley, W. Geochemistry and tectonics of the Crescent volcanic rocks, Olympic Peninsula, Washington. *Geol. Soc. Am. Bull.* **1974**, *85*, 785–794. [[CrossRef](#)]
45. Sun, S.S.; McDonough, W.F. Chemical and isotopic systematics of oceanic basalts: Implications for mantle compositions and processes. In *Magmatism in the Ocean Basins*; Saunders, A.D., Norry, M.J., Eds.; Geological Society of London: London, UK, 1989; Volume 42, pp. 313–345.
46. Wen, D.R.; Chung, S.L.; Song, B.; Lizuka, Y.; Yang, H.J.; Ji, J.Q.; Liu, D.Y.; Gallet, S. Late Cretaceous Gangdese intrusions of adakitic geochemical characteristics, SE Tibet: Petrogenesis and tectonic implications. *Lithos* **2008**, *105*, 1–11. [[CrossRef](#)]
47. Ma, L.; Wang, B.D.; Jiang, Z.Q.; Wang, Q.; Li, Z.X.; Wyman, D.A.; Zhao, S.R.; Yang, J.H.; Gou, G.N.; Guo, H.F. Petrogenesis of the Early Eocene adakitic rocks in the Napuri area, southern Lhasa: Partial melting of thickened lower crust during slab break-off and implications for crustal thickening in southern Tibet. *Lithos* **2014**, *196–197*, 321–338. [[CrossRef](#)]
48. Wang, R.Q.; Qiu, J.S.; Yu, S.B.; Lin, L.; Xu, H. Magma mixing origin for the Quxu intrusive complex in southern Tibet: Insights into the early Eocene magmatism and geodynamics of the southern Lhasa subterrane. *Lithos* **2019**, *328*, 14–32. [[CrossRef](#)]
49. Ding, L.; Kapp, P.; Wan, X.Q. Paleocene–Eocene record of ophiolite obduction and initial India–Asia collision, south central Tibet. *Tectonics* **2005**, *24*, TC3001. [[CrossRef](#)]
50. Wang, Z.Z.; Zhao, Z.D.; Asimow, P.D.; Li, X.P.; Meng, Y.K.; Liu, D.; Mo, X.X.; Zhu, D.C.; Tang, Y.; Cong, F.Y. Two episodes of Eocene mafic magmatism in the southern Lhasa terrane imply an eastward propagation of slab breakoff. *Gondwana Res.* **2022**, *110*, 31–43. [[CrossRef](#)]
51. Shu, C.T.; Long, X.P.; Yin, C.Q.; Yuan, C.; Wang, Q.; He, X.L.; Zhao, B.S.; Huang, Z.Y. Continental crust growth induced by slab breakoff in collisional orogens: Evidence from the Eocene Gangdese granitoids and their mafic enclaves, South Tibet. *Gondwana Res.* **2018**, *64*, 35–49. [[CrossRef](#)]
52. Liu, Z.C.; Wu, F.Y.; Ji, W.Q.; Liu, C.Z. Petrogenesis of the Ramba leucogranite in the Tethyan Himalaya and constraints on the channel flow model. *Lithos* **2014**, *208*, 118–136. [[CrossRef](#)]
53. Hou, Z.Q.; Zheng, Y.C.; Zeng, L.S.; Gao, L.E.; Huang, K.X.; Li, W.; Li, Q.Y.; Fu, Q.; Liang, W.; Sun, Q.Z. Eocene–Oligocene granitoids in southern Tibet: Constraints on crustal anatexis and tectonic evolution of the Himalayan orogen. *Earth Planet. Sci. Lett.* **2012**, *349–350*, 38–52. [[CrossRef](#)]
54. Shervais, J.W. Ti–V plots and the petrogenesis of modern and ophiolitic lavas. *Earth Planet. Sci. Lett.* **1982**, *59*, 101–118. [[CrossRef](#)]
55. Pearce, J.A. Geochemical fingerprinting of oceanic basalts with applications to ophiolite classification and the search for Archean oceanic crust. *Lithos* **2008**, *100*, 14–48. [[CrossRef](#)]
56. Hawkesworth, C.; Turner, S.; Peate, D.; McDermott, F.; Carstere, P. Elemental U and Th variations in island arc rocks: Implications for U-series isotopes. *Chem. Geol.* **1997**, *139*, 207–221. [[CrossRef](#)]
57. Zheng, H.; Huang, Q.T.; Kapsiotis, A.; Xia, B.; Yin, Z.X.; Zhong, Y.; Lu, Y.; Shi, X.L. Early Cretaceous ophiolites of the Yarlung Zangbo suture zone: Insights from dolerites and peridotites from the Baer upper mantle suite, SW Tibet (China). *Int. Geol. Rev.* **2017**, *59*, 1471–1489. [[CrossRef](#)]
58. Zhang, S.Q.; Mahoney, J.J.; Mo, X.X.; Ghazi, A.M.; Milani, L.; Crawford, A.J.; Guo, T.Y.; Zhao, Z.D. Evidence for a widespread Tethyan upper mantle with Indian-ocean-type isotopic characteristics. *J. Petrol.* **2005**, *46*, 829–858. [[CrossRef](#)]

59. Xu, J.F.; Castillo, P.R. Geochemical and Nd-Pb isotopic characteristics of the Tethyan asthenosphere: Implications for the origin of the Indian Ocean mantle domain. *Tectonophysics* **2004**, *393*, 9–27. [[CrossRef](#)]
60. Mahoney, J.J.; Frei, R.; Tejada, M.L.G.; Mo, X.X.; Leat, P.T.; Nägler, T.F. Tracing the Indian Ocean mantle domain through time: Isotopic results from old West Indian, East Tethyan, and South Pacific seafloor. *J. Petrol.* **1998**, *39*, 1285–1306. [[CrossRef](#)]
61. Gao, Y.F.; Yang, Z.S.; Hou, Z.Q.; Wei, R.H.; Meng, X.J.; Tian, S.H. Eocene potassic and ultrapotassic volcanism in south Tibet: New constraints on mantle source characteristics and geodynamic processes. *Lithos* **2010**, *117*, 20–32. [[CrossRef](#)]
62. Liu, F.; Yang, J.S.; Dilek, Y.; Xu, Z.Q.; Liang, F.H.; Chen, S.Y.; Lian, D.Y. Geochronology and geochemistry of basaltic lavas in the Dongbo and Purang ophiolites of the Yarlung-Zangbo Suture zone: Plume-influenced continental margin-type oceanic lithosphere in southern Tibet. *Gondwana Res.* **2015**, *27*, 701–718. [[CrossRef](#)]
63. Zhao, X.Y.; Yang, Z.S.; Yang, Y.; Cao, Y.; Fan, J.B.; Zhao, M. Discovery of Early Cretaceous metamorphic basic rock and plagioclase amphibolite in Yalaxiangbo, Tibet and its geological significance. *Earth Sci. Front.* **2023**, *30*, 163–182.
64. Guillot, S.; De Sigoyer, J.; Lardeaux, J.M.; Mascle, G. Eclogitic metasediments from the Tso Moriri area (Ladakh, Himalaya): Evidence for continental subduction during India-Asia convergence. *Contrib. Mineral. Petrol.* **1997**, *128*, 197–212. [[CrossRef](#)]
65. White, L.T.; Lister, G.S. The collision of India with Asia. *J. Geodyn.* **2012**, *56*, 7–17. [[CrossRef](#)]
66. van Hinsbergen, D.J.J.; Kapp, P.; Dupont-Nivet, G.; Lippert, P.C.; DeCelles, P.G.; Torsvik, T.H. Restoration of Cenozoic deformation in Asia and the size of Greater India. *Tectonics* **2011**, *30*, TC5003. [[CrossRef](#)]
67. Patriat, P.; Achache, J. India-Eurasia collision chronology has implications for crustal shortening and driving mechanism of plates. *Nature* **1984**, *311*, 615–621. [[CrossRef](#)]
68. Alam, M.G.M.; Snow, E.T.; Tanaka, A. Arsenic and heavy metal contamination of vegetables grown in Samta village, Bangladesh. *Sci. Total Environ.* **2003**, *308*, 83–96. [[CrossRef](#)]
69. Parrish, R.R.; Gough, S.J.; Searle, M.P.; Waters, D.J. Plate velocity exhumation of ultrahigh-pressure eclogites in the Pakistan Himalaya. *Geology* **2006**, *34*, 989–992. [[CrossRef](#)]
70. Negredo, A.M.; Replumaz, A.; Villaseñor, A.; Guillot, S. Modeling the evolution of continental subduction processes in the Pamir-Hindu Kush region. *Earth Planet. Sci. Lett.* **2007**, *259*, 212–225. [[CrossRef](#)]
71. Huang, Y.; Cao, H.W.; Li, G.M.; Brueckner, S.M.; Zhang, Z.; Dong, L.; Dai, Z.W.; Liu, L.; Li, Y.B. Middle-Late Triassic bimodal intrusive rocks from the Tethyan Himalaya in South Tibet: Geochronology, petrogenesis and tectonic implications. *Lithos* **2018**, *318*, 78–90. [[CrossRef](#)]
72. Lin, B.; Wang, L.Q.; Tang, J.X.; Song, Y.; Cao, H.W.; Baker, M.J.; Zhang, L.J.; Zhou, X. Geology, geochronology, geochemical characteristics and origin of Baomai porphyry Cu (Mo) deposit, Yulong Belt, Tibet. *Ore Geol. Rev.* **2018**, *92*, 186–204. [[CrossRef](#)]
73. Zhao, J.X.; Li, G.M.; Evans, N.J.; Qin, K.Z.; Li, J.X.; Zhang, X.N. Petrogenesis of Paleocene-Eocene porphyry deposit-related granitic rocks in the Yaguila-Sharang ore district, central Lhasa terrane, Tibet. *J. Asian Earth Sci.* **2016**, *129*, 38–53. [[CrossRef](#)]
74. Zhao, J.X.; Qin, K.Z.; Li, G.M.; Li, J.; Xiao, B.; Chen, L.; Yang, Y.H.; Li, C.; Liu, Y.S. Collision-related genesis of the Sharang porphyry molybdenum deposit, Tibet: Evidence from zircon U–Pb ages, Re–Os ages and Lu–Hf isotopes. *Ore Geol. Rev.* **2014**, *56*, 312–326. [[CrossRef](#)]
75. Zheng, Y.Y.; Sun, X.; Gao, S.B.; Zhao, Z.D.; Zhang, G.Y.; Wu, S.; You, Z.M.; Li, J.D. Multiple mineralization events at the Jiru porphyry copper deposit, southern Tibet: Implications for Eocene and Miocene magma sources and resource potential. *J. Asian Earth Sci.* **2014**, *79*, 842–857. [[CrossRef](#)]
76. Yang, Z.M.; Hou, Z.Q.; Chang, Z.S.; Li, Q.Y.; Liu, Y.F.; Qu, H.C.; Sun, M.Y.; Xu, B. Cospatial Eocene and Miocene granitoids from the Jiru Cu deposit in Tibet: Petrogenesis and implications for the formation of collisional and postcollisional porphyry Cu systems in continental collision zones. *Lithos* **2016**, *245*, 243–257. [[CrossRef](#)]
77. Luo, C.H.; Wang, R.; Weinberg, R.F.; Hou, Z.Q. Isotopic spatial-temporal evolution of magmatic rocks in the Gangdese belt: Implications for the origin of Miocene post-collisional giant porphyry deposits in southern Tibet. *Geol. Soc. Am. Bull.* **2022**, *134*, 316–324. [[CrossRef](#)]
78. Wang, R.; Richards, J.P.; Hou, Z.Q.; Yang, Z.M.; DuFrane, S.A. Increased magmatic water content—The key to Oligo-Miocene porphyry Cu–Mo ± Au formation in the eastern Gangdese belt, Tibet. *Econ. Geol.* **2014**, *109*, 1315–1339. [[CrossRef](#)]
79. Zhang, Z.M.; Ding, H.X.; Palin, R.M.; Dong, X.; Tian, Z.L.; Chen, Y.F. The lower crust of the Gangdese magmatic arc, southern Tibet, implication for the growth of continental crust. *Gondwana Res.* **2020**, *77*, 136–146. [[CrossRef](#)]

**Disclaimer/Publisher’s Note:** The statements, opinions and data contained in all publications are solely those of the individual author(s) and contributor(s) and not of MDPI and/or the editor(s). MDPI and/or the editor(s) disclaim responsibility for any injury to people or property resulting from any ideas, methods, instructions or products referred to in the content.